



Deposited via The University of Sheffield.

White Rose Research Online URL for this paper:

<https://eprints.whiterose.ac.uk/id/eprint/189044/>

Version: Published Version

Article:

Wingham, J., Ahmed, I., Islam, M.T. et al. (2022) Tailored additives for incorporation of antibacterial functionality into laser sintered parts. *Frontiers in Biomaterials Science*, 1. 929006.

<https://doi.org/10.3389/fbiom.2022.929006>

Reuse

This article is distributed under the terms of the Creative Commons Attribution (CC BY) licence. This licence allows you to distribute, remix, tweak, and build upon the work, even commercially, as long as you credit the authors for the original work. More information and the full terms of the licence here:

<https://creativecommons.org/licenses/>

Takedown

If you consider content in White Rose Research Online to be in breach of UK law, please notify us by emailing eprints@whiterose.ac.uk including the URL of the record and the reason for the withdrawal request.



Tailored Additives for Incorporation of Antibacterial Functionality Into Laser Sintered Parts

James R. Wingham¹, Ifty Ahmed², Md Towhidul Islam³, Joanna Shepherd⁴ and Candice Majewski^{1*}

¹Department of Mechanical Engineering, The University of Sheffield, Sheffield, United Kingdom, ²Faculty of Engineering, Advanced Materials Research Group, University Nottingham, Nottingham, United Kingdom, ³School of Physical Sciences, University of Kent, Canterbury, United Kingdom, ⁴School of Clinical Dentistry, The University of Sheffield, Sheffield, United Kingdom

OPEN ACCESS

Edited by:

Cristina Scielzo,
San Raffaele Hospital (IRCCS), Italy

Reviewed by:

Dan Ioan Stoia,
Politehnica University of Timisoara,
Romania
Swee Leong Sing,
National University of Singapore,
Singapore

*Correspondence:

Candice Majewski
c.majewski@sheffield.ac.uk

Specialty section:

This article was submitted to
Bioinspired and Complex Materials,
a section of the journal
Frontiers in Biomaterials Science

Received: 26 April 2022

Accepted: 09 June 2022

Published: 08 July 2022

Citation:

Wingham JR, Ahmed I, Islam MT,
Shepherd J and Majewski C (2022)
Tailored Additives for Incorporation of
Antibacterial Functionality Into Laser
Sintered Parts.
Front. Front. Biomater. Sci. 1:929006.
doi: 10.3389/fbiom.2022.929006

Infectious disease is a major cause of death worldwide, and novel methods capable of controlling the spread of disease are in high demand. This research presents a method of producing antimicrobial microcomposites by exploiting the powder-based nature of the Laser Sintering Additive Manufacturing process, via the incorporation of silver-containing additives. Silver phosphate glass additives in different formulations were designed to determine the effect of dissolution rate on the antimicrobial efficacy. These were characterised and successfully incorporated into polyamide 12 parts, without affecting the mechanical properties. The printed microcomposite parts displayed both bactericidal and antibiofouling effects against Gram-positive and Gram-negative bacteria in nutrient-poor conditions, with the efficacy found to be more sensitive to silver content than degradation rate.

Keywords: polymer laser sintering, antibacterial material, phosphate glass, microcomposite, additive manufacturing

1 INTRODUCTION

Additive Manufacturing (AM) is increasingly being used for the production of functional, end-use parts; now constituting 33.7% of its applications, and with an estimated \$2.21 billion spent on these in 2021 (Wohlers et al., 2022). Covering a range of different processes, AM can be defined as the “process of joining materials to make parts from 3D model data, usually layer upon layer, as opposed to subtractive manufacturing and formative manufacturing technologies” (ISO/ASTM, 2021). First commercialised over 30 years ago, Laser Sintering (LS), a powder bed fusion process, is now well established as an AM technology; building parts by spreading thin layers of a powder feedstock, then selectively melting the material in each layer to form consecutive cross-sections of the printed part (Goodridge et al., 2012). With its ability to create complex geometries throughout the build volume without the need for support structures, LS is well suited to the manufacture of functional parts; ranging from one-off commissions and functional prototypes, to batch or mass production of end-use products. As a process LS is now relatively well understood, with substantial current research focusing on broadening the potential applications of LS by introducing new materials and adding new functionality into printed parts.

Polyamides (including PA12, PA11, and PA6) have long since dominated the market for polymer powder bed fusion (PBF) processes such as LS (Redwood et al., 2018), and have been reported to be the most profitable AM polymer (Wohlers et al., 2022). This is reflected in the availability of

materials, with 61% of currently available polymer powder feedstocks being polyamide-based, of which 46% contain additional additives (or fillers) to create a composite feedstock (Senvol, 2022). These additives can be used to alter the mechanical properties of the parts [e.g., carbon fibres for increased strength (Yan et al., 2011), or glass beads for increased stiffness (Seltzer et al., 2011)], increase the processability of the powder during printing [e.g., silica for enhancing powder flow (Verbelen et al., 2016), carbon black for increased laser energy absorption (Wagner et al., 2004)], or to add new functionality into printed parts [e.g., a brominated hydrocarbon to add flame resistance (Booth et al., 2012)]. The subject of much academic and industrial interest (Wang et al., 2017; Yuan et al., 2019), these composites allow the tailoring of material properties without many of the challenges associated with processing a new base polymer.

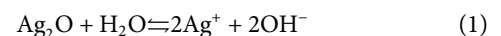
Alongside this, the spread of infectious disease is at the centre of global attention, and awareness of the need for new methods to control the spread of disease has never been higher. Exacerbated by the overuse of antibiotics, antimicrobial resistance (AMR) has become a major cause of death worldwide, responsible for 1.27 million deaths in 2019 and predicted to rise to 10 million a year by 2050 (Interagency Coordination Group on Antimicrobial Resistance, 2019; Antimicrobial Resistance Collaborators, 2022). To tackle this issue (and in addition to conserving antimicrobial efficacy by practising good antimicrobial stewardship only using antibiotics where appropriate), the largest impact can be made by controlling the spread of disease, thus reducing the initial level of infection and the subsequent need for treatment (O'Neill, 2016). Antimicrobial (antibacterial when dealing specifically with bacteria) materials could prove an effective tool for this, creating surfaces on which microbes are unable to survive, thereby reducing the potential routes of transmission for disease (Page et al., 2009). This can be especially effective for frequently used touchpoints, or equipment with complex or inaccessible parts which would otherwise be difficult to clean.

Antibacterial materials can be grouped into three main categories, based on how they react with bacteria. Anti-adhesive surfaces function by preventing the attachment of bacteria to the surface, avoiding or delaying the formation of biofilms¹ without harming the bacteria; contact-active surfaces cause cell death upon contact with the material, generally either through surface geometry or through anchoring antimicrobials to the surface; and biocide-releasing surfaces, which release antimicrobials into their surroundings to create a bactericidal effect, a category dominated by metal-containing surfaces releasing antimicrobial metal ions (Page et al., 2009; Campoccia et al., 2013; Adlhart et al., 2018). Antimicrobial metal-containing materials are starting to emerge in AM, with research into copper, zinc and silver-filled materials for material extrusion (Muwaffak et al., 2017; Tiimob et al., 2017; Zhang et al.,

2017) as well as commercially available filaments (Copper3D, 2022); with further research into silver-containing resins for vat photopolymerisation processes (such as stereolithography) (Taormina et al., 2018). In LS, the only commercial instance of an antimicrobial material is the proprietary PEKK material (OsteoFab technology) from Oxford Performance Materials (Maandi et al., 2020), primarily marketed for use in surgery to create bone scaffolds; with its surface geometry creating anti-adhesive and contact-active effects. Research has also been carried out into biocide-releasing LS PA12 parts (Turner et al., 2020), made by incorporating a commercially available phosphate-based silver-containing additive in the powder feedstock to create intrinsically antimicrobial parts.

Despite being used for thousands of years for its antimicrobial properties, the mechanisms by which silver acts against bacteria are not yet fully understood (Chernousova and Epple, 2013). Biologically inert in its metallic form (Möhler et al., 2018), its notoriety instead stems from the silver ions (Ag^+) which attack cells both directly (through disruption of the cell membrane, depletion of cellular thiols, ion mimicry, and destruction of Fe-S clusters) and indirectly (as the destroyed Fe-S clusters release Fe^{2+} and create cell damaging reactive oxygen species through the Fenton reaction) (Lemire et al., 2013; Palza, 2015). These ions are generally formed by reacting with water, a property that can be exploited by hygroscopic (able to absorb water) polymers such as polyamides to create antimicrobial materials. Silver-containing additives can be incorporated into the parts, with the absorbed water able to react with them and release Ag^+ ; this then diffuses throughout the part and into the surroundings, creating an intrinsically antimicrobial material (Palza, 2015). With the diffusion of water through polymers generally a slow process, the use of carrier materials for silver can be used to increase or further control the release of Ag^+ . Carriers such as zeolites can increase the Ag^+ release rate by aiding the water permeation into the composite part, through the generation of more free voids or by reducing the crystallinity of the polymer (Kumar et al., 2005). The speed of the reaction with the additives can also be increased (compared to with metallic silver) by including silver in a different form (such as silver oxide Ag_2O), to achieve equivalent or even faster rates of Ag^+ release, even with a lower total silver content (Palza, 2015; Mulligan et al., 2003; Kumar et al., 2005).

For silver oxide, the release of Ag^+ is governed by Eq. 1, in which the forward reaction (to create the silver ions) occurs in neutral or acidic solutions (Johnston et al., 1933).



To further tailor the release of Ag^+ , silver oxide can be combined with other oxides to create a glass. Phosphate (P_2O_5) based glasses are used in biomedical applications for their ability to dissolve completely in water, while controlling the release of antimicrobials such as silver (Ahmed et al., 2019). In its pure form phosphate dissolves quickly, however by adding other oxides (such as Na_2O , CaO , and MgO) in varying proportions, the release rate can be tailored to the desired application; creating an approximately linear dissolution rate

¹Biofilms are multilayered communities of bacteria which are usually heterogeneous in species composition, and are far less sensitive to antimicrobials than their free swimming (planktonic) counterparts.

TABLE 1 | Additive oxide compositions by molar percentage, with the designed formulation shown alongside the measured value from EDX (shown in brackets—raw data in supplementary information).

Glass Name (abbreviation)	Designed Glass Formulation (Measured Value)/ molar%				
	P ₂ O ₅	MgO	CaO	Na ₂ O	Ag ₂ O
P40Mg24Ca16Na18Ag2 (P40)	40 (42)	24 (25)	16 (14)	18 (17)	2 (2)
P45Mg19Ca16Na18Ag2 (P45)	45 (48)	19 (19)	16 (15)	18 (16)	2 (2)
P50Mg14Ca16Na18Ag2 (P50)	50 (52)	14 (14)	16 (15)	18 (18)	2 (2)
B65003 ^a	(48)	(34)	(17)	–	(1)

^acommercial additive—calculated from the measurements in (Turner et al., 2020).

(and associated release of Ag⁺) over its lifetime (Mulligan et al., 2003; Ahmed et al., 2006).

This research aims to exploit the customisability of silver-doped phosphate-based glasses to create additives for Laser Sintering, and more deeply understand their effectiveness in manufacturing intrinsically antibacterial printed parts with LS. A method for producing the tailored additives is presented here, with the experiments designed to validate the method of production, and evaluate the antibacterial efficacy of the printed microcomposite parts. While there are obvious potential applications of this approach in healthcare settings (e.g., for complex invasive medical devices), there are likely to be additional applications throughout a wider range of industries (e.g., consumer goods).

2 MATERIALS AND METHODS

2.1 Overview

The research presented here builds on the work carried out by Turner et al. (2020), investigating the effects of altering the additive degradation rate on the antimicrobial efficacy of LS PA12 microcomposite parts. Here, three silver-doped phosphate-based glass formulations were developed based on the commercially available additive analysed by Turner et al. (2020). The proportions of P₂O₅ and MgO were altered to create glass compositions with different degradation rates; with decreased levels of P₂O₅ and increased levels of MgO both previously shown to reduce the degradation rate in water (Gao et al., 2004; Lee et al., 2013). The amounts of Ag₂O were designed to be kept constant, as increasing this has also been shown to affect the structure of phosphate-based glasses, increasing their strength and decreasing degradation rates (Ahmed et al., 2006, 2007; Moss et al., 2008).

The glasses were milled into powders and characterised, before being combined with PA12 powder to create composite feedstocks suitable for LS. All three feedstocks were successfully processed with LS, creating microcomposite parts with three different compositions. The mechanical properties of the microcomposites were determined and compared to pure PA12 parts, and the surface composition analysed. Finally the antimicrobial efficacy of the three microcomposites was investigated against both Gram-positive

and Gram-negative bacteria, with their bactericidal (ability to kill bacteria) and antibiofouling (ability to prevent or reduce biofilm formation) investigated in both contact and non-contact environments.

2.2 Powder Characterisation and 3D Printing

2.2.1 Production of Silver-Containing Additives

Three silver-doped phosphate-based glass formulations were developed to assess the effect of degradation rate on the antimicrobial efficacy of the printed parts; these were based on the measured composition of a commercial additive (B65003—BioCote (Turner et al., 2020)), the manufacturer's measurement of silver content in B65003 (1.9%), and personal experience. The chosen glasses were in the system of (50-*x*)P₂O₅-(14 + *x*)MgO-16CaO-18Na₂O-2Ag₂O (where *x* = 0, 5, 10), as shown in Table 1. The intended degradation rate was altered by varying the amount of phosphate in the glasses, with a higher phosphate content expected to lead to a faster degradation rate. This was used to denote the three formulations as P40, P45, and P50.

To manufacture the glasses, the precursors (NaH₂PO₄, MgHPO₄·3H₂O, CaHPO₄, P₂O₅—Sigma Aldrich, Ag₃PO₄—Alfa Aesar) were weighed and mixed to achieve the formulations in Table 1, before being transferred to a quartz crucible (VWR International) and placed in a furnace. Ordinarily, a platinum crucible would be used for glass production; however, to avoid any possibilities of the silver alloying with the platinum, quartz crucibles were instead used. The precursors were heated at a rate of 10°C/min, held at 350°C for 0.5 h to remove any H₂O, then heated further and held at 1,150°C for 1.5 h to achieve full melting. The resulting molten glass was then poured onto a steel plate and allowed to cool to room temperature. The glass was subsequently ground using a Retsch PM 100 ball mill, and sieved to obtain a < 45 μm particle size.

2.2.2 Characterisation of Silver-Containing Additives

In order to verify the composition of the additives produced, Energy-dispersive X-ray Spectroscopy (EDX) was used. For this, a small amount of each powder was attached to self-adhesive carbon pads, gold sputter-coated, and imaged using a TESCAN VEGA3 SEM, the attached Oxford EDX analysis and associated software (AZtec, Oxford Instruments). An accelerating voltage of 15 kV was used, with back scattered electrons measured to

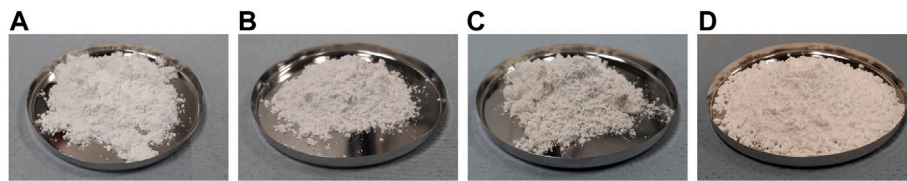


FIGURE 1 | Photos of the three custom silver phosphate glass additives produced, each amount shown is approximately 20 g. Showing **(A)** P40, **(B)** P45, **(C)** P50, **(D)** commercial additive B65003.

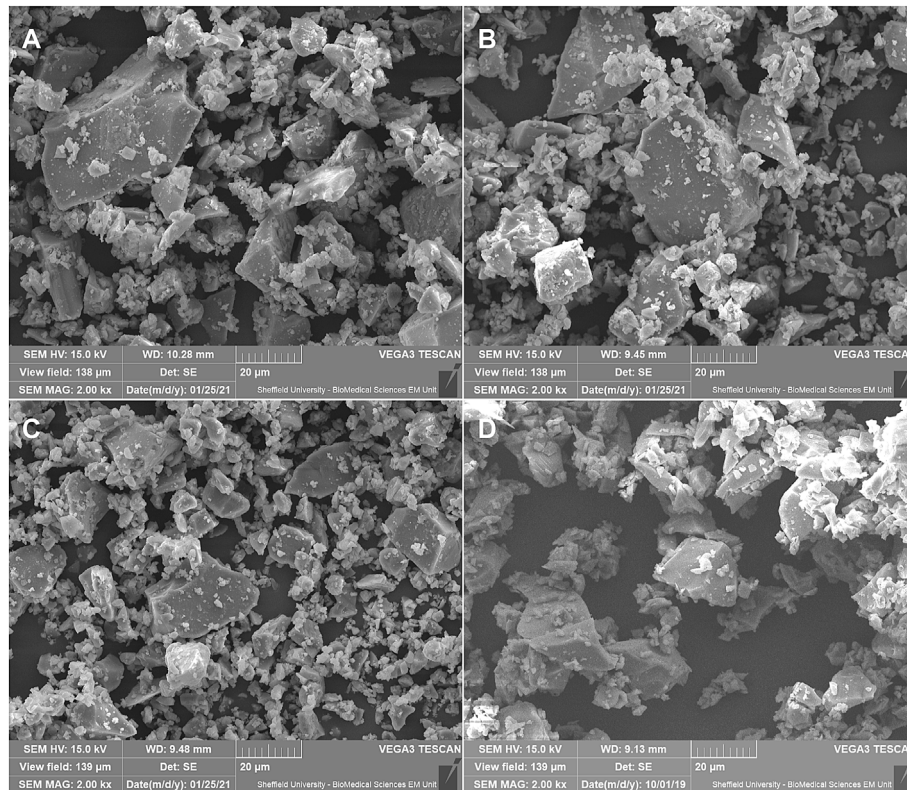


FIGURE 2 | SEM images of the phosphate-based glass additives at $\times 2,000$ magnification. Showing **(A)** P40 (custom-made) **(B)** P45 (custom-made) **(C)** P50 (custom-made), and **(D)** B65003 (commercial).

highlight differences in the material composition. The measured weight% compositions were converted to atomic% using their atomic mass (PubChem, 2020), with the molar% of the oxides calculated from the atomic% of each element (P, Mg, Ca, Na, Ag).

To characterise the morphology of the powders, Scanning Electron Microscopy (SEM) was carried out alongside the EDX analysis using the same samples and equipment. For this, a 15 kV accelerating voltage was again used, detecting scattered electrons to clearly view the particle shape.

To obtain a statistically significant size distribution, the powders were measured using a Mastersizer 3,000 laser diffraction particle size analyser. A dry dispersion unit was used to analyse the soluble phosphate glass powders, and a refractive index of 1.627 used. From this, the volume-based diameter metrics of D10, D50, and D90 (10,

50, and 90% along the cumulative distribution) were recorded, along with the average diameter weighted by volume (D [4,3]).

2.2.3 Laser Sintering

For each additive, a composite feedstock was created by adding 1% by weight to virgin polyamide 12 powder (PA2200—EOS). This was subsequently mixed in a rotary tumbler (EOS—mixing station P1) for approximately 100 min, with three acrylic blocks added to enhance mixing.

Test specimens were printed using an EOS Formiga P100 LS machine, with the default “performance” parameters for PA2200 used (Pfefferkorn and Weilhammer, 2017); these being laser power 21 W, scan spacing 0.25 mm, scan speed 2,500 mm/s, layer height 100 μm , bed temperature 170°C, with no contours

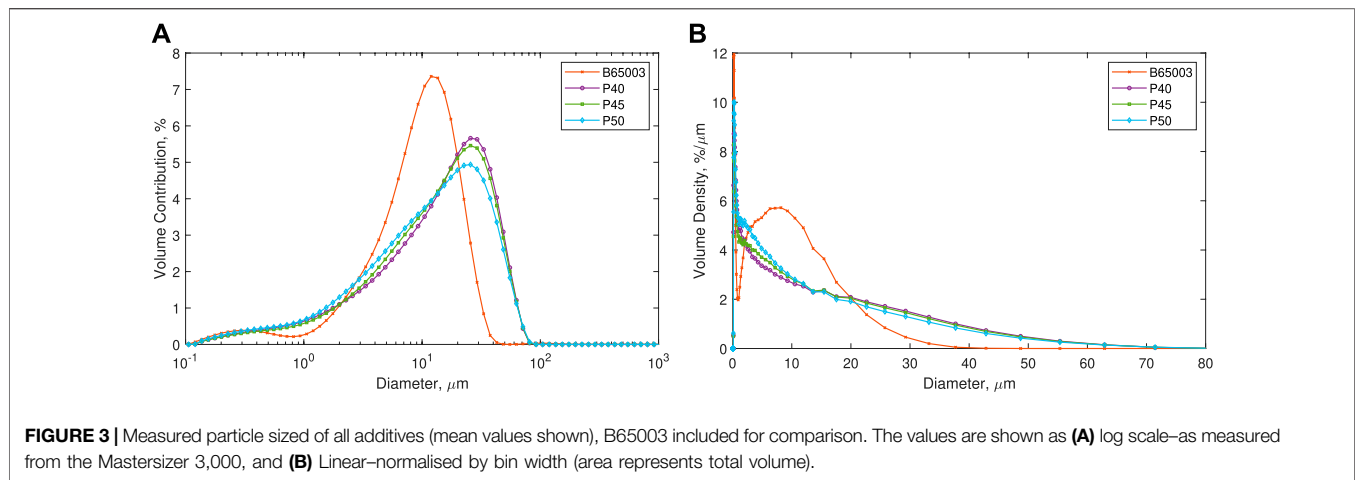


TABLE 2 | Results of the particle size analysis of the additives.

Glass Additive	D10/ μm	D50/ μm	D90/ μm	D [4,3]/ μm	Weighted Residual/ %
P40	1.93 ± 0.07	15.5 ± 0.2	41.3 ± 0.9	18.9 ± 0.3	0.58 ± 0.04
P45	2.10 ± 0.02	14.8 ± 0.1	40.6 ± 0.6	18.5 ± 0.2	0.56 ± 0.09
P50	1.74 ± 0.02	13.0 ± 0.1	39.4 ± 0.4	17.2 ± 0.1	0.83 ± 0.17
B65003	2.48 ± 0.04	9.83 ± 0.07	21.1 ± 0.4	11.1 ± 0.5	0.81 ± 0.04

used. The same build layout and parameters were used for all four builds; tensile specimens were oriented in the x-direction (XYZ according to ISO/ASTM (2016)), with the laser alternately scanning layers at 0° and 90° to the direction of testing. Excess powder was removed from all parts using compressed air only to reduce any potential contamination.

2.3 Characterisation of Printed Microcomposites

Tensile testing was used to determine the mechanical properties of the printed parts; with the Young's modulus (E), ultimate tensile strength (σ_{uts}), and elongation at break (ϵ_{max}) used to characterise the parts. All testing was carried out in accordance with ASTM D638 (ASTM International, 2014), with $5 \times$ type I specimens tested per material. Testing was carried out on a Tinius Olsen 5K with Laser Extensometer, at a rate of 5 mm/min.

In order to qualitatively check the additive incorporation and dispersion on the part surface, SEM and EDX of the part surfaces were carried out. This utilised the same setup as for the additive analysis (see Section 2.2.2), with an accelerating voltage of 15 kV used and detecting back-scattered electrons. A whole area element map was obtained for the microcomposite parts, allowing for the identification of the additives and any other features on the part surface.

2.4 Antibacterial Testing

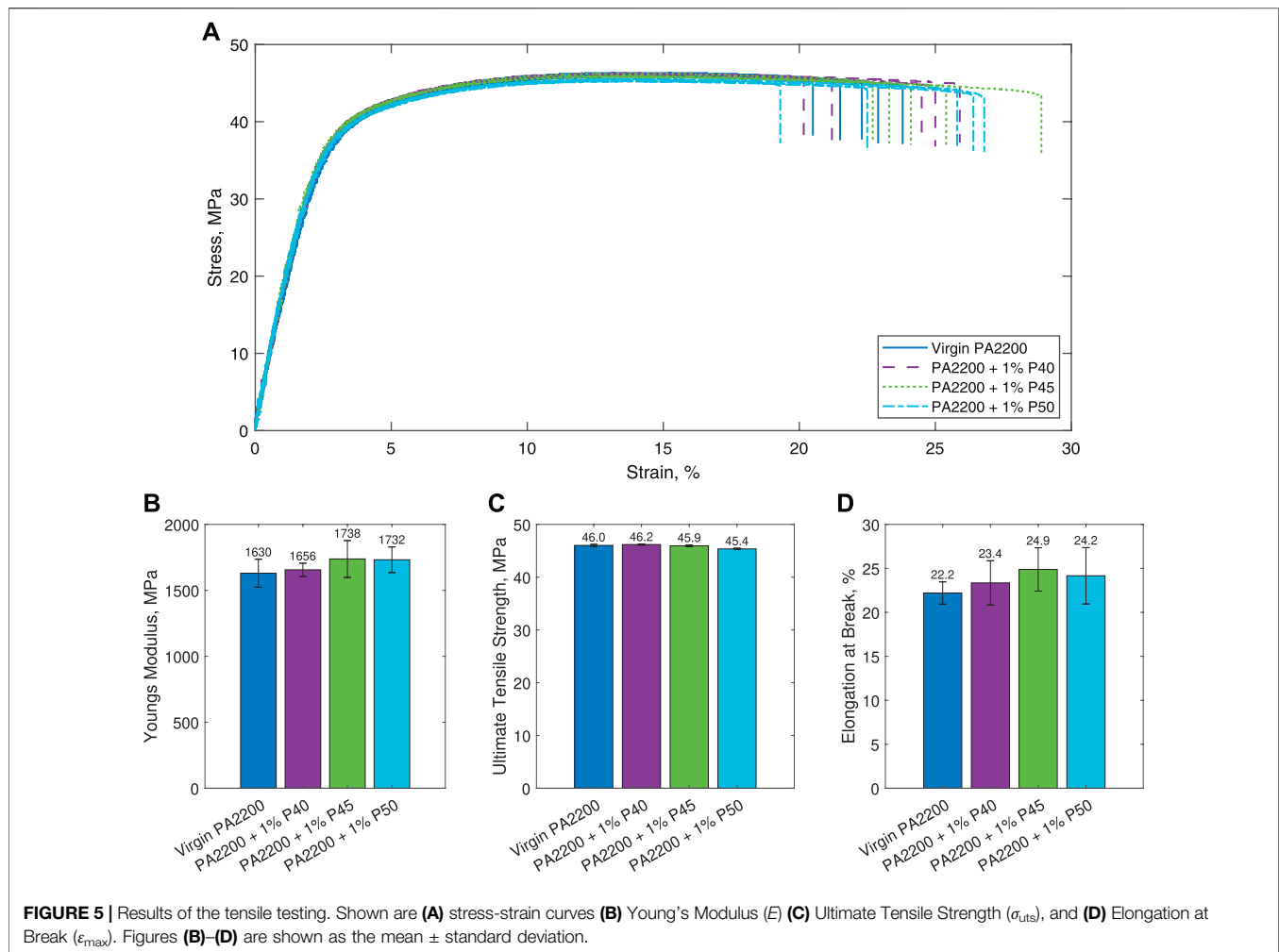
2.4.1 Bacterial Strains

The bacteria used were clinical isolate strains of the Gram-positive, methicillin-resistant *Staphylococcus aureus* S235

(MRSA—referred to as *S. aureus*), and Gram-negative *Pseudomonas aeruginosa* SOM1 (referred to as *P. aeruginosa*), provided by the Charles Clifford Dental Hospital, Sheffield. Both of these are examples of commonly found, biofilm forming bacteria, which can cause significant infection, especially in immunocompromised patients. Bacteria were maintained on stock Brain Heart Infusion (BHI) agar plates stored at 4°C . For experimental use, single colonies were picked from the plate, suspended in 15 ml BHI broth and incubated overnight at 37°C in a shaking incubator before use.



FIGURE 4 | Photo of the equivalent part from all three builds containing the custom additives and one without additives. Shown are (top to bottom), virgin PA2200 + 1% P50, virgin PA2200 + 1% P45, virgin PA2200 + 1% P40, virgin PA2200.



2.4.2 Powder Antibacterial Efficacy

Before testing the efficacy of the microcomposite parts, the additives were tested in isolation to determine the maximum possible effectiveness. In order to maintain a direct comparison with the part testing, conditions were identical to those used in part testing (see **Section 2.4.3**); with the mass of additive (approximately 10 mg) representative of the amount in a 1 cm³ part at 1% by weight.

The custom glasses were weighed out into glass universals to an accuracy of 10–12 μ g, before being sterilised (in a steam autoclave at 121°C); three samples were prepared per material per repeat. The chosen bacteria were grown in BHI, with the overnight cultures diluted to an OD₆₀₀ of 0.01 in Phosphate Buffered Saline (PBS); 5 ml of these were added to each sample and incubated in a shaking incubator (150 RPM at 37°C) for 24 h. Following this, 10 μ L of the powder/bacteria suspension was taken from each sample and a Miles and Misra serial dilution carried out to determine the number of CFUs, an indication of the number of viable bacteria present in the sample. This protocol is shown graphically in the **Supplementary Information**.

2.4.3 Contact Antibacterial Efficacy

The protocol described here was designed to replicate those used by Turner et al. (2020), with some changes included to increase reliability and allow for a higher throughput of samples. These included adding a negative control (no microcomposite part) and reducing the volume of the serial dilutions spotted onto agar (5 μ L compared to 20 μ L) to enable testing of a large number of samples simultaneously. Spherical 1 cm³ samples were printed from each material for these tests, including samples made from pure PA2200 for comparison.

Three spheres per material per repeat were used, with each one placed in a glass universal and sterilised (steam autoclave at 121°C) before use. Bacteria were grown overnight in BHI before being diluted to an OD₆₀₀ of 0.01 in PBS; 5 ml of which was added to each sample and incubated in a shaking incubator (either 150, 175 or 210 RPM depending on availability, at 37°C) for 24 h.

After incubation, 10 μ L of the surrounding media was taken from each sample to measure the unadhered planktonic bacteria, with a Miles and Misra serial dilution carried out to determine the number of CFUs. To isolate the biofilm attached to the part surface,

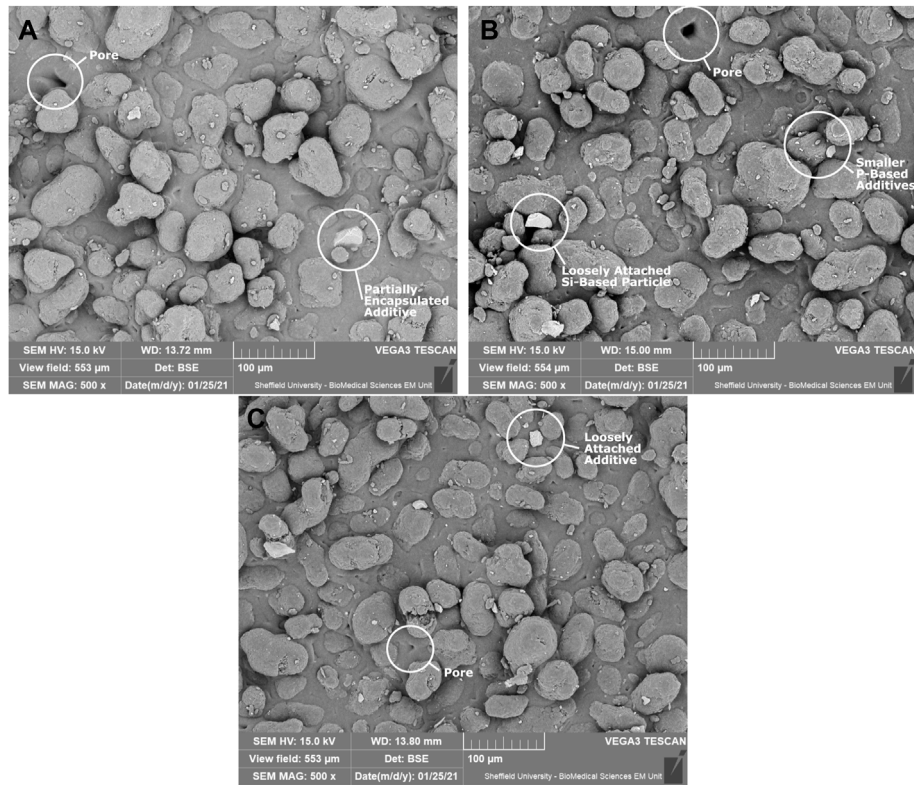


FIGURE 6 | SEM images of the microcomposite surfaces containing the custom additives. The brighter features are additives, with the majority of the smaller features over the entire surface found to be the custom-made phosphorus-based additives. All features identified were found on all three materials. Shown are **(A)** 1% P40 Part **(B)** 1% P45 Part, and **(C)** 1% P50 Part.

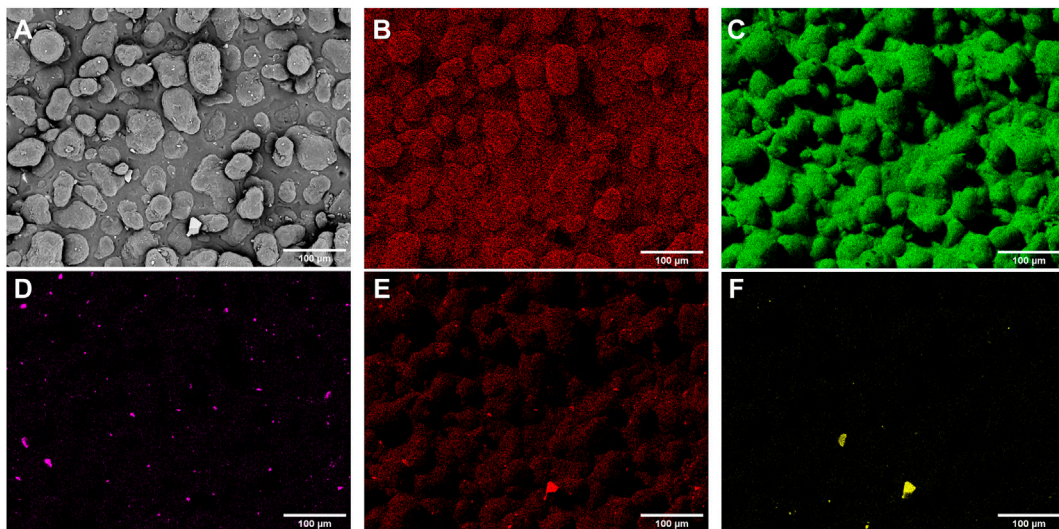
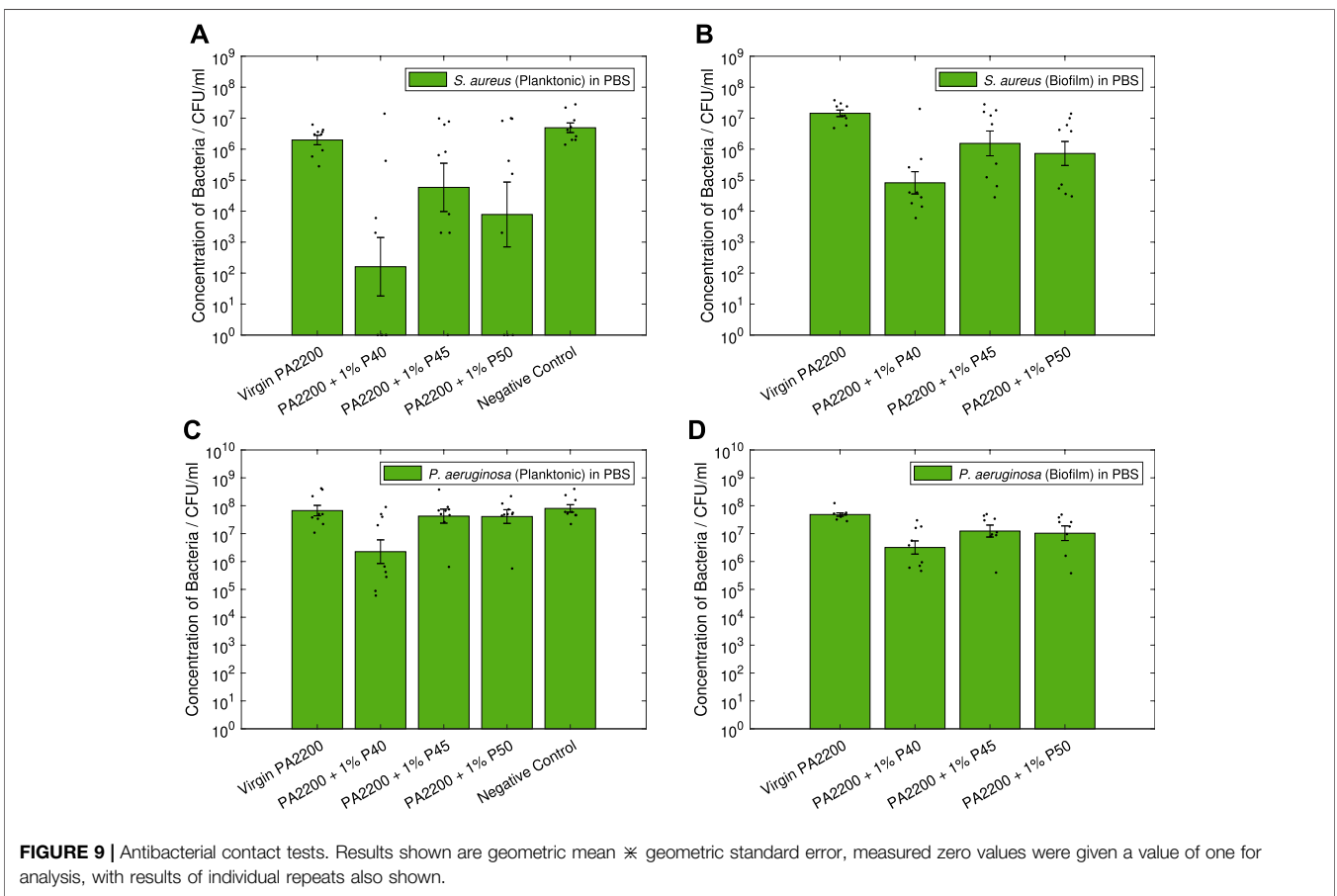
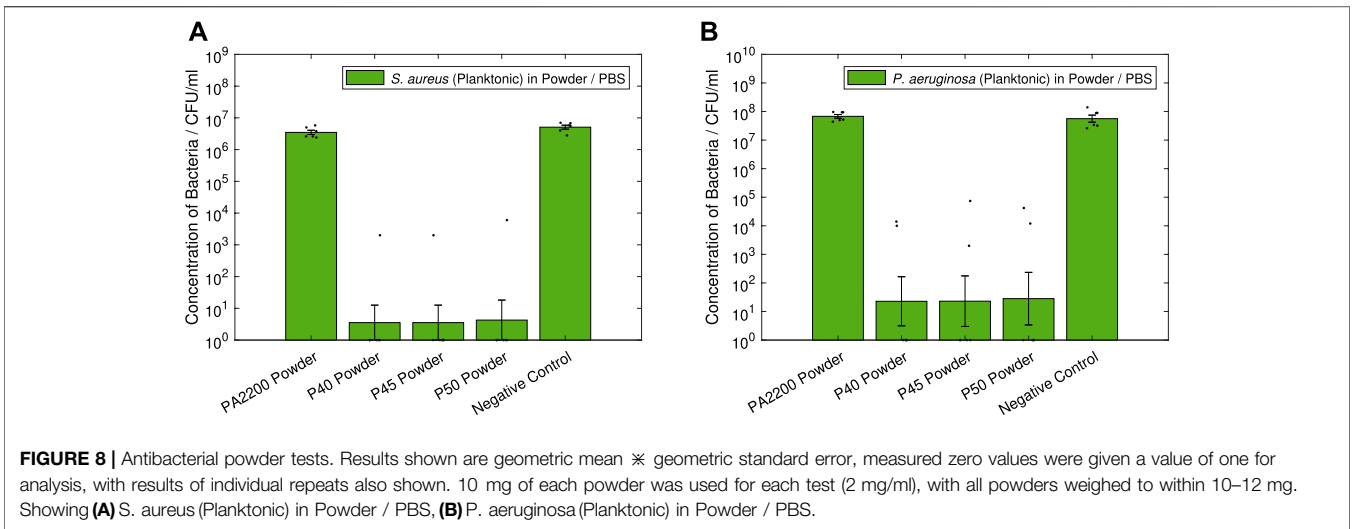


FIGURE 7 | SEM and elemental maps on the surface of a 1% P50 microcomposite part obtained with EDX, with phosphorus indicative of the additive location. Shown are **(A)** SEM image **(B)** Gold **(C)** Carbon **(D)** Phosphorus **(E)** Oxygen, and **(F)** Silicon. Additional maps for Calcium, Magnesium and Titanium are not shown, with the concentration of silver too low to be detected.

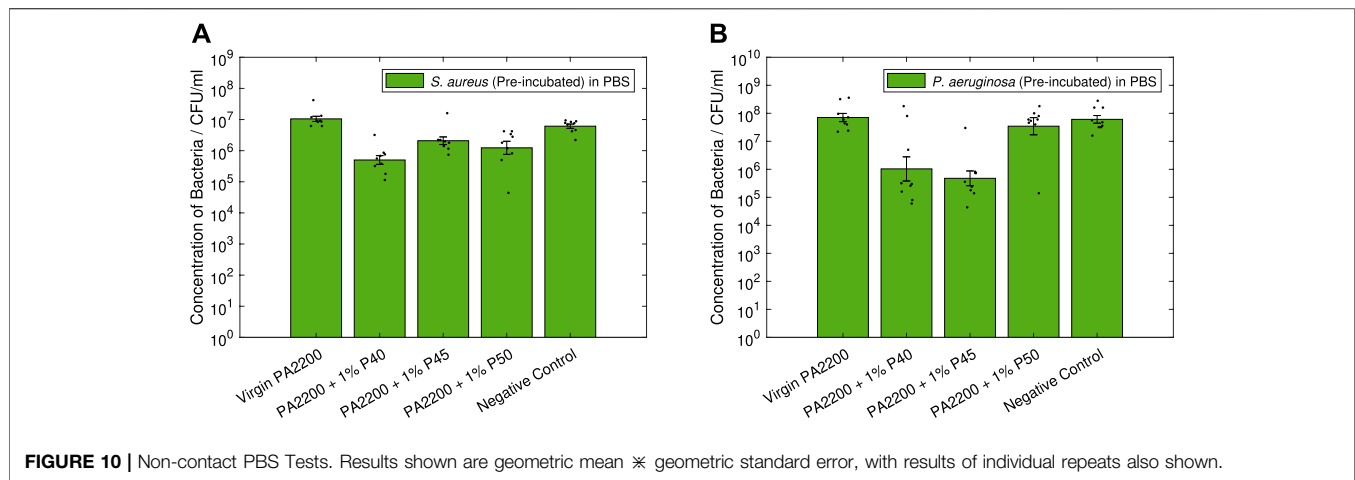


the remaining media was removed and each sphere rinsed twice with fresh PBS (5 ml each time) to remove loosely attached cells. 2 ml PBS was then added and each sphere was vortexed at the highest setting for 30 s to remove the attached biofilm. 10 μ L of the resulting suspension was removed, with a Miles and Misra serial dilution carried out to count the CFUs. This protocol is shown graphically in the **Supplementary Information**.

2.4.4 Non-Contact Antibacterial Efficacy

The non-contact protocols were again based on those used by Turner et al. (2020), with the same modification made as for the contact protocol (see **Section 2.4.3**).

Printed 1 cm³ spheres were used, with three spheres used per material per repeat; these were placed in glass universals and sterilised (steam autoclave at 121°C) before use. For the non-



contact testing, 5 ml PBS was added to each sample and incubated in a shaking incubator (150 RPM at 37°C) for 24 h, after which the spheres were removed. The bacteria (*P. aeruginosa* and *S. aureus*—grown overnight in BHI), were then added into each universal to an OD₆₀₀ of 0.01. These were incubated for a further 24 h in a shaking incubator (150 RPM at 37°C) for 24 h, after which 10 μ L of each suspension was removed, and a Miles and Misra dilution carried out to count the CFUs. This protocol is shown graphically in the **Supplementary Information**.

3 RESULTS

3.1 Powder Characterisation and 3D Printing

3.1.1 Additive Production

Photos of the three tailored additives produced are shown in **Figure 1**, where all the powders appear white in colour and similar to one another.

3.1.2 Additive Composition

The oxide molar% compositions of the additives are shown in **Table 1**, calculated from the weight% measured in EDX scanning (data available in the **Supplementary Information**). The data from Turner et al. (2020) has also been used here to calculate the composition of B65003 using the same method. Here it can be seen that the measured silver content (Ag₂O) was higher for P40 than anticipated, and slightly lower for both P45 and P50.

3.1.3 Powder Morphology

SEM images of the custom-made powdered glass additives can be seen in **Figure 2**, alongside a scan of the commercially available B65003 for comparison in **Figure 2D**. In these, all four powders can be seen to be similar in both size and shape.

3.1.4 Particle Size

The results of the particle size analysis are shown in **Figure 3**, with key values shown in **Table 2**; the values for B65003 have been included here for comparison. Here it can be seen that the three

tailored additives are very similar to one another, and broadly comparable to the commercial additive.

3.1.5 Laser Sintering

All the parts printed without any observable issues (such as curl or excessive smoking), validating the use of the standard PA2200 parameters. For the scanned areas of the build, there was a noticeable difference in colour for the additive-containing powders (see **Supplementary Information**), although this did not appear to affect the build. Photos of post-processed parts containing the custom additives can be seen in **Figure 4**.

3.2 Microcomposite Properties

3.2.1 Mechanical Properties

The results of the tensile testing can be seen in **Figure 5**, both as the raw stress-strain curves (**Figure 5A**) and comparing the measured values of E , σ_{uts} , and ϵ_{max} (**Figures 5B–D**). No obvious decrease in the mechanical properties can be seen for any of the microcomposite parts compared to the pure PA12 parts.

A 2-sample Welch's t -test was used to determine whether there were any statistically significant differences in the measured values, where a p value of $p < 0.05$ indicates the means are significantly different. The only statistically significant difference identified from this was the σ_{uts} for 1% P50, which showed a 0.6 MPa decrease ($p < 0.001$) compared to PA2200.

3.2.2 Surface Composition

SEM images of parts containing the three custom additives are shown in **Figure 6**, with key features annotated. The elemental maps from EDX for a part containing 1% P50 are shown in **Figure 7**, with the maps of gold, carbon, phosphorus, oxygen, and silicon shown. In these, the gold is a result of the sputter-coating of the samples, the carbon is present in the polyamide 12 polymer matrix, the phosphorus and oxygen maps (in combination with calcium and magnesium—not shown) are indicative of the additive location, and the silicon and titanium maps are thought to be additional additives in the PA2200 powder from the manufacturer as well as post-printing contaminants.

3.3 Antibacterial Testing

3.3.1 Powder Antibacterial Efficacy

The results from the powder antibacterial testing can be seen in **Figure 8**, where all of the silver phosphate glass powders can be seen to be extremely effective against both *S. aureus* and *P. aeruginosa*. A Welch's *t*-test was used, with values of $p < 0.05$ deemed to be statistically significant.

In **Figure 8A**, all of the glass powders can be seen to have a significant antimicrobial effect on *S. aureus*; with large reductions in CFU/ml measured for P40 (6.0-log, $p < 0.001$), P45 (6.0-log, $p < 0.001$) and P50 (5.9-log, $p < 0.001$) compared to pure PA12. A similarly large effect can be seen in **Figure 8B** against *P. aeruginosa*, with 6.5-log ($p = 0.001$), 6.5-log ($p = 0.001$) and 6.4-log ($p = 0.001$) reductions measured for P40, P45 and P50 respectively. It is worth noting that for both strains of bacteria, the PA2200 powder showed no significant difference to the negative controls.

3.3.2 Contact Antibacterial Efficacy

Results of the contact testing for *S. aureus* are shown in **Figures 9A,B**, showing the planktonic and biofilm data respectively. In the planktonic data (**Figure 9A**), reductions compared to PA2200 can be seen for all the microcomposites, with 4.1-log, 1.5-log and 2.4-log reductions seen for 1% P40, 1% P45 and 1% P50 respectively. However with the variation measured, only 1% P40 showed a statistically significant reduction ($p = 0.002$), with 1% P50 only just above the 0.05 threshold ($p = 0.051$). All the microcomposites showed a significant reduction compared to the negative control. The *S. aureus* biofilm data (shown in **Figure 9B**), shows statistically significant reductions for all of the microcomposites compared to PA2200; showing a large decrease for 1% P40 (2.2-log, $p < 0.001$), and slightly smaller reductions for 1% P45 (1.0-log, $p = 0.043$) and 1% P50 (1.3-log, $p = 0.010$).

The results of the contact efficacy test for *P. aeruginosa* are shown in **Figures 9C,D**, for the planktonic and biofilm data respectively. In the planktonic data (**Figure 9C**), it can be seen that all the microcomposites display a small reduction in CFU compared to PA2200, with the only statistically significant reduction measured in 1% P40 (1.5-log, $p = 0.009$). Similarly for the biofilm data in **Figure 9D**, 1% P40 shows the largest reduction in CFU (1.2-log, $p = 0.001$), with smaller but still statistically significant differences measured in 1% P45 (0.6-log, $p = 0.025$) and 1% P50 (0.7-log, $p = 0.039$).

3.3.3 Non-Contact Antibacterial Efficacy

The results of the non-contact testing can be seen in **Figure 10** for both *S. aureus* and *P. aeruginosa*.

In **Figure 10A**, the microcomposites can all be seen to have statistically significant effect against *S. aureus*. Here it can be seen that 1% P40 shows the largest reduction in CFU (1.3-log, $p < 0.001$), followed by 1% P50 (0.9-log, $p = 0.002$) and 1% P45 (0.7-log, $p < 0.001$).

For *P. aeruginosa* (**Figure 10B**), only two of the microcomposites were seen to have a significant effect on the CFU. In this, 1% P45 can be seen to have the largest reduction (2.2-log, $p < 0.001$) followed by 1% P40 (1.8-log, $p = 0.002$), no significant difference can be seen for 1% P50.

4 DISCUSSION

4.1 Powder Characterisation and 3D Printing

4.1.1 Additive Composition

The measured compositions of the tailored additives (**Table 1**), show a slight deviation from the designed formulations. Of these, the phosphate (P_2O_5 —affecting the additive dissolution rate) and silver (Ag—affecting the total amount of Ag^+ which can be released) content were likely to be the most important in terms of the antimicrobial efficacy. For these reasons in the design of the glasses, the silver content was kept constant, with the compositions allowing for comparison of slow (P40), medium (P45), and fast (P50) degrading phosphate-based glass additives. The measured phosphate values for P40, P45 and P50 (42, 48, and 52%) were deemed sufficient to enable the comparison between different degradation rates.

The silver content of the three glasses also deviated from the expected values (expected to be 2%), with 5% by weight measured for P40, 4% for P45, and 3% for P50. This suggests that although P40 was expected to dissolve the slowest, the increased silver content could counteract this (as was the case in (Ahmed et al., 2007)), increasing the release rate of Ag^+ and its subsequent antimicrobial efficacy.

4.1.2 Powder Morphology

In the SEM images of the glass powders (shown in **Figure 2**), all three compositions can be seen to be very similar in both shape and size. The morphology is also very similar to that of the commercial B65003 additive (**Figure 2D**), with the distinctive jagged edges and irregularly sized particles.

In terms of the performance of these additives, this similarity was essential for comparing the chemical compositions, rather than the morphology or particle size. The SEM images shown here suggest that the manufacturing processes used to create the powders were consistent between the glasses, and reduces the likelihood of particle size or shape being the cause of any differences in the antimicrobial efficacy.

4.1.3 Particle Size

In the manufacture of the powders, a standard sieve size of 45 μm was used, which although slightly larger than the $< 40 \mu m$ specification of B65003, matched it as closely as possible. As expected, all three of the custom glasses were shown to be larger in size than the commercial additive (see **Table 2**), with the average particle sizes (D_{50}) measured as 13.0–15.5 μm compared to 9.8 μm .

The shape of the distributions can also be seen to be different in **Figure 3**, with a longer tail off in the custom glasses and a greater proportion of smaller particles were measured compared to B65003. This difference was suspected to be due to additional sieving steps carried out commercially, removing smaller particles to be sold separately. In the production of the tailored additives here, the dramatic reduction in the yield this would bring, coupled with the increased production time and high cost of consumables, meant that this was impractical to replicate.

Comparing the custom glasses to each other, the shape of the distributions (**Figure 3**) can be seen to be very similar for all three,

with a subtly smaller size measured for P50. Although this slight difference could affect the efficacy of the powder, this would only act to increase the dissolution rate, which was already intended to be the highest in P50. Considering both this and the overwhelming similarities between the distributions, the results shown here suggest that the particle size is not likely to significantly affect the antimicrobial efficacy of the powders.

4.2 Microcomposite Properties

4.2.1 Mechanical Properties

The stress-strain plots (**Figure 5A**), show that all the materials follow a very similar profile with no major differences between any of the specimens tested. This is supported by the values of E , σ_{uts} , and ϵ_{max} (**Figures 5B–D**), which again show very similar values for all the materials. A Welch's t -test shows that the only statistically significant difference from the PA2200 specimens is the value of σ_{uts} for 1% P50 ($p < 0.001$). However, it is important to note that although statistically significant, this only represents a difference of 0.6 MPa. Practically, this would not be sufficient a decrease in properties to warrant changing the design in the majority of applications.

Although the tensile results presented here suggest the differences in the mechanical properties are small, it is worth noting that this only represents the specific LS parameters, sample orientation, additive loading, and surface finishing described in **Section 2.2.3**. It is known that altering individual parameters in the printing process (especially those affecting the Energy Density, including laser power, scan speed and scan spacing) will have significant effects on the tensile properties of the printed parts (Pilipović et al., 2018). Equally, the orientation and laser scanning strategy will also have a large effect on the tensile properties and fracture toughness of any parts produced (Stoia et al., 2019, 2020), which cannot be assumed to be similarly unaffected by the inclusion of the additives.

4.2.2 Surface Composition

The SEM images of the microcomposites (**Figures 6A–C**), show a number of key features one would expect to see on the surface of LS parts; these being a combination of partially melted powder particles, fully melted areas, and “open” pores in the fully melted areas. As expected for a microcomposite material, both partially encapsulated and loosely attached additive particles were seen in every material. This shows that the additives had been successfully incorporated into the parts, with no obvious effects on the microstructure at the surface. Due to the similarities with the commercial additive, the tailored additives were expected to be similarly randomly dispersed throughout the volume of the parts; with the dispersion previously extensively explored by Wingham et al. (2020) and Turner et al. (2020).

Combining these with EDX measurements (such as those in **Figure 7**), it was possible to further characterise the additives in the SEM images. For all the scans, phosphate-based particles were identified across the surface, suggesting that feedstock preparation was sufficient and the additives were relatively evenly dispersed. In some images, larger, loosely attached, silicon-based particles were also detected (see **Figures 6B,C** – compositions identified with EDX). Since none of these were

detected encapsulated in the parts, these were suspected to be contamination after printing, possibly during powder removal or in transport to SEM scanning; these were not thought to affect the performance of the parts.

In these experiments, the post-processing affecting the part surface comprised solely of powder removal using compressed air jets. This represents the default surface finish of LS parts, which is generally followed by additional post-processing (such as media blasting or vapour smoothing) to alter the finish and surface roughness of the parts (Tamburrino et al., 2021). With such a wide range of additional post-processing methods used in industry (each with the potential to affect the initial adhesion of bacteria to the surface, the release rate of Ag^+ from the part, and introduce other factors or contaminants), further testing should be carried out for any additional surface finishing to determine both the effects on the mechanical properties and the antimicrobial efficacy.

4.3 Antibacterial Testing

4.3.1 Powder Antibacterial Efficacy

For all three of the custom additives tested, the reduction in both *S. aureus* and *P. aeruginosa* measured (**Figure 8**) shows the powders are extremely antimicrobial, typically displaying a 6-log reduction or more in the measured CFUs. This quantifies the upper limit of the effectiveness expected from the microcomposite parts; however, since such a large difference was detected for all the powders, they were all predicted to have at least some antimicrobial effect.

During testing, the four powders could each be seen to react differently over the 24 h incubation. As expected, the PA2200 powder was not visibly affected. However for P40 and P45, these agglomerated together during autoclaving, with P40 turning a darker colour, likely due to the increased silver content and subsequent oxidation. P50 was not distinguishable as a powder after 24 h incubation, suggesting that (as per the additive design) this dissolved much more quickly. Although not quantifiable, this suggests that the designed differences in phosphate content for the three glass additives did result in significantly different dissolution rates.

4.3.2 Contact Antibacterial Efficacy

4.3.2.1 Antimicrobial Efficacy

For all the microcomposites, an antimicrobial effect against both *S. aureus* and *P. aeruginosa* was measured in the contact efficacy testing. In all tests (contact and non-contact), a general trend was observed of 1% P40 showing the largest antimicrobial efficacy, followed by 1% P50, and 1% P45 the least effective.

The only microcomposite to consistently show statistically significant reductions in CFU (planktonic and biofilm) was 1% P40, consistently outperforming the other glasses (**Figure 9**). This can be explained based on the measured composition of the glasses (**Section 2.2.2**), where P40 was found to contain a much higher amount of silver (5% by weight) compared to P45 and P50 (4 and 3%). Interestingly, this increase in performance was observed despite P40 being (theoretically, based on the measured phosphorus content) the slowest to dissolve of the three glasses. This suggests that the difference in silver content between the glasses was sufficient enough to negate the effects of a slower dissolution rate.

Whereas only 1% P40 showed significant reduction in CFU for the planktonic bacteria, all the microcomposites showed

statistically significant reductions in the biofilm formation on the parts (**Figures 9B,D**). As expected, the biofilm data for both *S. aureus* and *P. aeruginosa* show the same trends as the planktonic data, with a clear link between the two aspects. However the variability in the results for the biofilms was lower than the planktonic, particularly for PA2200, resulting in the lower *p*-values measured. In **Figure 9C**, 1% P45 and 1% P50 can be seen to have a negligible effect on planktonic *P. aeruginosa*; similarly for the biofilm data (**Figure 9D**), although statistically significant, the reductions here are small (0.6-log and 0.7-log), only showing a limited effect on the biofilms.

4.3.2.2 Sample Variation

In all of the tests (most notably in **Figure 9A**), a large spread in the measured CFU count can be seen for the microcomposite parts. As this variation was larger in the microcomposite samples than with PA2200 or the control, this was thought arise from differences in the antimicrobial efficacy of the individual spheres, rather than with the bacteria or the experimental method. The additive dispersion in the parts could be the cause of this, with the possibility that in some of the spheres there was a higher concentration of the glass near the surface. However, the mixing method and similarities to the commercial additives analysed by Wingham et al. (2020) strongly suggest the additives were dispersed throughout the bulk of the material. For this reason, any differences arising from this or the silver content of individual additive particles (which are potentially exacerbated by the short timescales) are expected to be mitigated as more of the part becomes saturated with water.

4.3.3 Non-Contact Antibacterial Efficacy

The non-contact tests shown in **Figure 10** clearly show that the microcomposite parts have an antimicrobial effect on the surrounding environment, even without contact with the surface. This supports the theory that the majority of this effect was due to the elution of Ag^+ into the surrounding media.

For *S. aureus*, the trend seen in **Figure 10A** is the same as the one seen with the contact tests, again with 1% P40 showing the largest reduction (1.3-log) in CFU. Despite all of the microcomposites showing statistically significant differences, the effect for 1% P45 and 1% P50 is lower (0.9-log and 0.7-log), again suggesting that the increased silver content of P40 outweighs the slower rate of dissolution.

Interestingly for *P. aeruginosa* (**Figure 10B**), the largest antimicrobial effect was observed with 1% P45 (2.2-log reduction), making it comparable to the efficacy of 1% P40 (1.8-log reduction). This stands in contrast to all the other antimicrobial testing carried out, suggesting that (although it is possible that other factors are in play), this could just be due to the random variation in the testing or the parts. As seen with the contact testing, 1% P50 showed no significant efficacy against *P. aeruginosa*.

5 CONCLUSION

This research presents a method of creating tailored microcomposites for use in Laser Sintering, to create

intrinsically antibacterial parts using Additive Manufacturing. The approach shows that though the use of silver-doped phosphate-based glasses, the properties of additives incorporated into the part can be tailored to an extent, with the silver content having the dominant effect on the part antibacterial efficacy. The printed microcomposite parts were found to be effective against representative strains of bacteria in nutrient-poor conditions, both against biofilm formation and planktonic cells. The incorporation of additives in the parts did not affect the mechanical properties, allowing for the addition of this functionality without the need for design alterations.

Future work should focus on the effect of additive loading, the effect of using different base polymers, and on determining the long-term effectiveness against a broad range of bacteria and other microbes.

DATA AVAILABILITY STATEMENT

The original contributions presented in the study are included in the article/**Supplementary Material**, further inquiries can be directed to the corresponding author.

AUTHOR CONTRIBUTIONS

JW, IA, and CM contributed to conception and design of the study. CM, JS, and IA provided resources and supervision. IA and MTI provided the phosphate-based glasses. JW and MTI carried out experimental work. JW wrote the first draft of the manuscript. All authors contributed to manuscript revision, read, and approved the submitted version.

FUNDING

Funded by The University of Sheffield Department of Mechanical Engineering Centenary Scholarship and the EPSRC Doctoral Training Partnership.

ACKNOWLEDGMENTS

This work is aligned with the EPSRC Future Manufacturing Hub in Manufacture using Advanced Powder Processes (EP/P006566/1). For the purpose of open access, the author has applied a Creative Commons Attribution (CC BY) licence to any Author Accepted Manuscript version arising.

SUPPLEMENTARY MATERIAL

The Supplementary Material for this article can be found online at: <https://www.frontiersin.org/articles/10.3389/fbiom.2022.929006/full#supplementary-material>

REFERENCES

- Adlhart, C., Verran, J., Azevedo, N. F., Olmez, H., Keinänen-Toivola, M. M., Gouveia, I., et al. (2018). Surface Modifications for Antimicrobial Effects in the Healthcare Setting: a Critical Overview. *J. Hosp. Infect.* 99, 239–249. doi:10.1016/j.jhin.2018.01.018
- Ahmed, A. A., Ali, A. A., and El-Fiqi, A. (2019). Glass-forming Compositions and Physicochemical Properties of Degradable Phosphate and Silver-Doped Phosphate Glasses in the P2O5-CaO-Na2O-Ag2O System. *J. Mater. Res. Technol.* 8, 1003–1013. doi:10.1016/j.jmrt.2018.07.012
- Ahmed, I., Abou Neel, E. A., Valappil, S. P., Nazhat, S. N., Pickup, D. M., Carta, D., et al. (2007). The Structure and Properties of Silver-Doped Phosphate-Based Glasses. *J. Mater. Sci.* 42, 9827–9835. doi:10.1007/s10853-007-2008-9
- Ahmed, I., Ready, D., Wilson, M., and Knowles, J. C. (2006). Antimicrobial Effect of Silver-Doped Phosphate-Based Glasses. *J. Biomed. Mat. Res.* 79A, 618–626. doi:10.1002/jbm.a.30808
- Antimicrobial Resistance Collaborators (2022). Global Burden of Bacterial Antimicrobial Resistance in 2019: a Systematic Analysis. *Lancet* 399, 629–655. doi:10.1016/S0140-6736(21)02724-0
- ASTM International (2014). *Standard Test Method for Tensile Properties of Plastics*. ASTM D638-14. doi:10.1520/D0638-14
- Booth, R. B., Thornton, B. C., Vanelli, D. L., and Gardiner, M. L. (2012). Methods and Systems for Fabricating Fire Retardant Materials. *U.S. Pat. No* 8236, 418.
- Campoccia, D., Montanaro, L., and Arciola, C. R. (2013). A Review of the Biomaterials Technologies for Infection-Resistant Surfaces. *Biomaterials* 34, 8533–8554. doi:10.1016/j.biomaterials.2013.07.089
- Chernousova, S., and Eppele, M. (2013). Silver as Antibacterial Agent: Ion, Nanoparticle, and Metal. *Angew. Chem. Int. Ed.* 52, 1636–1653. doi:10.1002/anie.201205923
- Copper3D (2022). Antimicrobial Performance. Available at: <https://copper3d.com/pages/antimicrobial-performance> (Accessed 02 14, 2022).
- Gao, H., Tan, T., and Wang, D. (2004). Effect of Composition on the Release Kinetics of Phosphate Controlled Release Glasses in Aqueous Medium. *J. Control. Release* 96, 21–28. doi:10.1016/j.jconrel.2003.12.030
- Goodridge, R. D., Tuck, C. J., and Hague, R. J. M. (2012). Laser Sintering of Polyamides and Other Polymers. *Prog. Mater. Sci.* 57, 229–267. doi:10.1016/j.pmatsci.2011.04.001
- Interagency Coordination Group on Antimicrobial Resistance (2019). *No Time to Wait: Securing the Future from Drug-Resistant Infections. Report to the Secretary-General of the U. N. World Health Organization.*
- ISO/ASTM (2021). *Additive Manufacturing – General Principles – Fundamentals and Vocabulary*. West Conshohocken: ISO/ASTM 52900, 2021.
- ISO/ASTM (2016). *Standard Terminology for Additive Manufacturing – Coordinate Systems and Test Methodologies*. ISO/ASTM 52921:2016.
- Johnston, H. L., Cuta, F., and Garrett, A. B. (1933). The Solubility of Silver Oxide in Water, in Alkali and in Alkaline Salt Solutions. The Amphoteric Character of Silver Hydroxide. *J. Am. Chem. Soc.* 55, 2311–2325. doi:10.1021/ja01333a016
- Kumar, R., Howdle, S., and Münstedt, H. (2005). Polyamide/silver Antimicrobials: Effect of Filler Types on the Silver Ion Release. *J. Biomed. Mat. Res.* 75B, 311–319. doi:10.1002/jbm.b.30306
- Lee, I.-H., Shin, S.-H., Foroutan, F., Lakhkar, N. J., Gong, M.-S., and Knowles, J. C. (2013). Effects of Magnesium Content on the Physical, Chemical and Degradation Properties in a MgO–CaO–Na2O–P2O5 Glass System. *J. Non-Crystalline Solids* 363, 57–63. doi:10.1016/j.jnoncrysol.2012.11.036
- Lemire, J. A., Harrison, J. J., and Turner, R. J. (2013). Antimicrobial Activity of Metals: Mechanisms, Molecular Targets and Applications. *Nat. Rev. Microbiol.* 11, 371–384. doi:10.1038/nrmicro3028
- Maandi, A., Porteus, J., and Roberts, B. (2020). OsteoFab Technology. *Whitepaper, Oxford Performance Materials*. Connecticut: South Windsor.
- Möhler, J. S., Sim, W., Blaskovich, M. A. T., Cooper, M. A., and Ziora, Z. M. (2018). Silver Bullets: A New Lustre on an Old Antimicrobial Agent. *Biotechnol. Adv.* 36, 1391–1411. doi:10.1016/j.biotechadv.2018.05.004
- Moss, R. M., Pickup, D. M., Ahmed, I., Knowles, J. C., Smith, M. E., and Newport, R. J. (2008). Structural Characteristics of Antibacterial Bioresorbable Phosphate Glass. *Adv. Funct. Mat.* 18, 634–639. doi:10.1002/adfm.200700721
- Mulligan, A. M., Wilson, M., and Knowles, J. C. (2003). Effect of Increasing Silver Content in Phosphate-Based Glasses on Biofilms of *Streptococcus Sanguis*. *J. Biomed. Mat. Res.* 67A, 401–412. doi:10.1002/jbm.a.10052
- Muwaffak, Z., Goyanes, A., Clark, V., Basit, A. W., Hilton, S. T., and Gaisford, S. (2017). Patient-specific 3D Scanned and 3D Printed Antimicrobial Polycaprolactone Wound Dressings. *Int. J. Pharm.* 527, 161–170. doi:10.1016/j.ijpharm.2017.04.077
- O'Neill, J. (2016). *Tackling Drug-Resistant Infections Globally: Final Report and Recommendations*. Tech. rep. London: Review on Antimicrobial Resistance.
- Page, K., Wilson, M., and Parkin, I. P. (2009). Antimicrobial Surfaces and Their Potential in Reducing the Role of the Inanimate Environment in the Incidence of Hospital-Acquired Infections. *J. Mat. Chem.* 19, 3819–3831. doi:10.1039/B818698G
- Palza, H. (2015). Antimicrobial Polymers with Metal Nanoparticles. *Ijms* 16, 2099–2116. doi:10.3390/ijms16012099
- Pfefferkorn, F., and Weilhammer, J. (2017). *Open and Flexible: EOS Part Property Management Provides Both Individualization and Standardization*. Munich, Germany: Whitepaper, EOS GmbH.
- Pilipović, A., Brajlilić, T., and Drstvenšek, I. (2018). Influence of Processing Parameters on Tensile Properties of SIs Polymer Product. *Polymers* 10, 1208. doi:10.3390/polym10111208
- PubChem (2020). *Periodic Table of Elements*. Available at: <https://pubchem.ncbi.nlm.nih.gov/periodic-table/> (Accessed 11 25, 2020).
- Redwood, B., Schöffner, F., and Garret, B. (2018). “3D Printing Technologies and Materials,” in *The 3D Printing Handbook – Technologies, Design and Applications* (Arnhem: Coers & Roest), 1, 16–143.
- Seltzer, R., de la Escalera, F. M., and Segurado, J. (2011). Effect of Water Conditioning on the Fracture Behavior of PA12 Composites Processed by Selective Laser Sintering. *Mater. Sci. Eng. A* 528, 6927–6933. doi:10.1016/j.msea.2011.05.045
- Senvol (2022). Senvol Database: Industrial Additive Manufacturing Machines and Materials. Available at: <http://senvol.com/database/> (Accessed 01 31, 2022).
- Stoia, D. I., Marşavina, L., and Linul, E. (2019). Correlations between Process Parameters and Outcome Properties of Laser-Sintered Polyamide. *Polymers* 11, 1850. doi:10.3390/polym11111850
- Stoia, D. I., Marsavina, L., and Linul, E. (2020). Mode I Fracture Toughness of Polyamide and Alumide Samples Obtained by Selective Laser Sintering Additive Process. *Polymers* 12, 640. doi:10.3390/polym12030640
- Tamburrino, F., Barone, S., Paoli, A., and Razionale, A. V. (2021). Post-processing Treatments to Enhance Additively Manufactured Polymeric Parts: a Review. *Virtual Phys. Prototyp.* 16, 221–254. doi:10.1080/17452759.2021.1917039
- Taormina, G., Sciancalepore, C., Bondioli, F., and Messori, M. (2018). Special Resins for Stereolithography: *In Situ* Generation of Silver Nanoparticles. *Polymers* 10, 212. doi:10.3390/polym10020212
- Tiimob, B. J., Mwinyelle, G., Abdela, W., Samuel, T., Jeelani, S., and Rangari, V. K. (2017). Nanoengineered Eggshell-Silver Tailored Copolyester Polymer Blend Film with Antimicrobial Properties. *J. Agric. Food Chem.* 65, 1967–1976. doi:10.1021/acs.jafc.7b00133
- Turner, R. D., Wingham, J. R., Paterson, T. E., Shepherd, J., and Majewski, C. (2020). Use of Silver-Based Additives for the Development of Antibacterial Functionality in Laser Sintered Polyamide 12 Parts. *Sci. Rep.* 10, 892. doi:10.1038/s41598-020-57686-4
- Verbelen, L., Dadbakhsh, S., Van den Eynde, M., Kruth, J.-P., Goderis, B., and Van Puyvelde, P. (2016). Characterization of Polyamide Powders for Determination of Laser Sintering Processability. *Eur. Polym. J.* 75, 163–174. doi:10.1016/j.eurpolymj.2015.12.014
- Wagner, T., Höfer, T., Knies, S., and Eyerer, P. (2004). Laser Sintering of High Temperature Resistant Polymers with Carbon Black Additives. *Int. Polym. Process.* 19, 395–401. doi:10.3139/217.1846
- Wang, X., Jiang, M., Zhou, Z., Gou, J., and Hui, D. (2017). 3d Printing of Polymer Matrix Composites: A Review and Prospective. *Compos. Part B Eng.* 110, 442–458. doi:10.1016/j.compositesb.2016.11.034
- Wingham, J. R., Turner, R., Shepherd, J., and Majewski, C. (2020). Micro-CT for Analysis of Laser Sintered Micro-composites. *Rpj* 26, 649–657. doi:10.1108/RPJ-08-2019-0211
- Wohlers, T., Campbell, I., Diegel, O., Kowen, J., and Mostow, N. (2022). *Wohlers Report 2022: 3D Printing and Additive Manufacturing Global State of the Industry*. Washington, DC: ASTM International.

- Yan, C., Hao, L., Xu, L., and Shi, Y. (2011). Preparation, Characterisation and Processing of Carbon Fibre/polyamide-12 Composites for Selective Laser Sintering. *Compos. Sci. Technol.* 71, 1834–1841. doi:10.1016/j.compscitech.2011.08.013
- Yuan, S., Shen, F., Chua, C. K., and Zhou, K. (2019). Polymeric Composites for Powder-Based Additive Manufacturing: Materials and Applications. *Prog. Polym. Sci.* 91, 141–168. doi:10.1016/j.progpolymsci.2018.11.001
- Zhang, Y., Zhai, D., Xu, M., Yao, Q., Zhu, H., Chang, J., et al. (2017). 3D-printed Bioceramic Scaffolds with Antibacterial and Osteogenic Activity. *Biofabrication* 9, 025037. doi:10.1088/1758-5090/aa6ed6

Conflict of Interest: The authors declare that the research was conducted in the absence of any commercial or financial relationships that could be construed as a potential conflict of interest.

Publisher's Note: All claims expressed in this article are solely those of the authors and do not necessarily represent those of their affiliated organizations, or those of the publisher, the editors and the reviewers. Any product that may be evaluated in this article, or claim that may be made by its manufacturer, is not guaranteed or endorsed by the publisher.

Copyright © 2022 Wingham, Ahmed, Islam, Shepherd and Majewski. This is an open-access article distributed under the terms of the Creative Commons Attribution License (CC BY). The use, distribution or reproduction in other forums is permitted, provided the original author(s) and the copyright owner(s) are credited and that the original publication in this journal is cited, in accordance with accepted academic practice. No use, distribution or reproduction is permitted which does not comply with these terms.